

# Highly Sensitive Terahertz Thin-Film Total Internal Reflection Spectroscopy Reveals in Situ Photoinduced Structural Changes in Methylammonium Lead Halide Perovskites

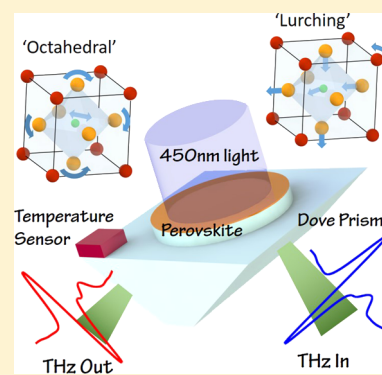
Qiushuo Sun,<sup>†,§</sup> Xudong Liu,<sup>†,§</sup> Jie Cao,<sup>†</sup> Rayko I. Stantchev,<sup>†</sup> Yang Zhou,<sup>†</sup> Xuequan Chen,<sup>†</sup> Edward P. J. Parrott,<sup>†</sup> James Lloyd-Hughes,<sup>‡,Ⓛ</sup> Ni Zhao,<sup>†,Ⓛ</sup> and Emma Pickwell-MacPherson<sup>\*,†,‡,Ⓛ</sup>

<sup>†</sup>Department of Electronic Engineering, The Chinese University of Hong Kong, Shatin, Hong Kong

<sup>‡</sup>Department of Physics, University of Warwick, Gibbet Hill Road, Coventry CV4 7AL, U.K.

## Supporting Information

**ABSTRACT:** Terahertz (THz) thin-film total internal reflection (TF-TIR) spectroscopy is shown to have an enhanced sensitivity to the vibrational properties of thin films in comparison with standard THz transmission spectroscopy. This increased sensitivity was used to track photoinduced modifications to the structure of thin films of methylammonium (MA) lead halide,  $\text{MAPbI}_{3-x}\text{Br}_x$  ( $x = 0, 0.5, 1, \text{ and } 3$ ). Initially, illumination strengthened the phonon modes around 2 THz, associated with Pb–I stretch modes coupled to the MA ions, whereas the 1 THz twist modes of the inorganic octahedra did not alter in strength. Under longer term illumination, the 1 THz phonon modes of encapsulated films slowly reduced in strength, whereas in films exposed to moisture and oxygen, these phonons weaken more rapidly and blue-shift in frequency. The rapid monitoring of environmentally induced changes to the vibrational modes afforded by TF-TIR spectroscopy offers applications in the characterization and quality control of the perovskite thin-film solar cells and other thin-film semiconductors.



## INTRODUCTION

The rapid development of organic–inorganic halide perovskite materials has facilitated their use in photovoltaic solar cells,<sup>1–3</sup> light-emitting diodes (LEDs),<sup>4</sup> and lasers.<sup>5</sup> However, concerns about the stability of halide perovskites have been raised as a major issue that obstructs their practical applications: water, oxygen, light, and heat can cause halide perovskites to degrade.<sup>1,2</sup> The degradation of perovskites can be slowed down by proper encapsulation or by partially replacing methylammonium (MA) with formamidinium.<sup>1</sup>

Above band gap illumination can alter the structural and functional electronic properties of the halide perovskites, even while remaining within the perovskite phase. In MA perovskites, the photoinduced carriers reduce the binding energy and increase the rotational freedom of the MA cation,<sup>6</sup> inducing a giant dielectric response.<sup>7</sup> UV illumination was found to alter the Raman lines and the photoluminescence (PL) intensity of  $\text{MAPbI}_3$  reversibly and was attributed to changes in the inorganic octahedra to adapt to light-induced rotations in the MA cations.<sup>8,9</sup> In the mixed halide perovskites, where the band gap can be tuned via the iodine to bromine ratio,<sup>10</sup> light can stimulate the halide ions to segregate into Br-rich and I-rich domains with different band gaps.<sup>11,12</sup>

Common vibrational spectroscopy methods such as Raman,<sup>13</sup> Fourier transform infrared spectroscopy,<sup>14</sup> and terahertz time-domain spectroscopy (THz-TDS)<sup>15,16</sup> have been widely utilized to study the vibrational modes of the perovskite crystalline lattice and the organic cation. THz-TDS

in particular is attractive, as it probes the low-frequency vibrational modes that dominate the electron–phonon scattering rate and thus the room temperature mobility.<sup>15,17</sup> Previously, THz-TDS was used to study the vibrational modes in the orthorhombic, tetragonal, and cubic phases of  $\text{MAPbX}_3$  perovskites<sup>16,17</sup> and to investigate the kinetics of  $\text{MAPbI}_3$  crystal formation from precursors during annealing.<sup>18</sup> In these experiments, standard THz-TDS transmission setups were utilized, typically yielding less than 10% amplitude change between sample and reference measurements for typical film thicknesses.<sup>16</sup> To obtain sufficiently precise spectrally resolved data, long integration times (>10 min) are often needed, restricting the usefulness of THz-TDS transmission spectroscopy to monitor environmentally induced changes in the vibrational modes of perovskite thin films on shorter time scales.

In this paper, we report that THz thin-film total internal reflection (TF-TIR) spectroscopy is a sensitive probe of the vibrational modes of perovskite thin films and validates the high sensitivity of this method. Utilizing this advance, we studied light-induced modifications to the vibrational modes of single and mixed halide  $\text{MAPbX}_3$ . Time-dependent changes in the vibrational mode strength, frequency, and linewidth were tracked under different environmental conditions. A thin-film

Received: June 14, 2018

Revised: June 27, 2018

Published: June 28, 2018

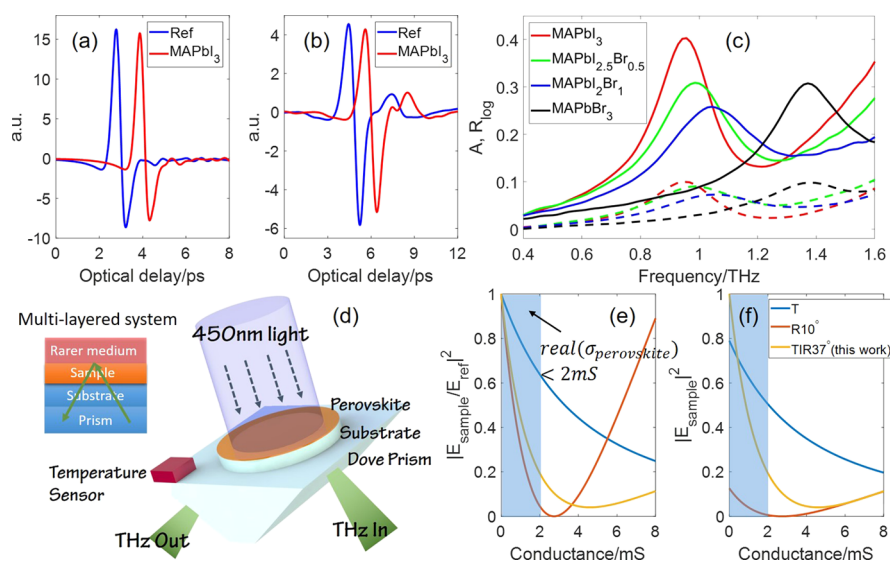


**Figure 1.** THz time-domain signals of a MAPbI<sub>3</sub> perovskite sample and the bare substrate measured in the (a) transmission system and (b) TF-TIR system. The sample signals are shifted horizontally for clarity. (c) Spectra of the pristine perovskite samples. Dashed lines were measured in transmission, whereas solid lines were measured by TF-TIR. (d) Dove prism setup for THz TF-TIR and schematic of the multilayered system in this setup. Green arrows show the optical paths of the THz light. (e) Normalized and (f) absolute THz amplitudes as a function of sheet conductance calculated by eq 1, assuming that the reference has a sample conductance of zero. “T”, “R”, and “TIR” correspond to transmission, ordinary reflection, and total internal reflection geometry.

encapsulation layer, made of fluoropolymer CYTOP, was optionally used to mitigate against the effects of exposure to moisture and oxygen. Complementary X-ray diffraction (XRD) and PL measurements of the perovskite thin-film samples under the same environmental conditions were used to monitor the structure and band-edge emission.

## RESULTS AND DISCUSSION

**Enhanced THz Responsivity by TF-TIR.** The THz time-domain signals of a pristine MAPbI<sub>3</sub> perovskite sample measured in transmission and in the TF-TIR geometry are shown in Figure 1a,b. In transmission, the THz pulse amplitude reduced by 5.4% in comparison with the reference substrate, whereas in the TF-TIR geometry, the signal change was larger, at 9.1%. The higher sensitivity of the TIR geometry to the conductivity of thin films in comparison with the transmission method has been previously established for graphene<sup>19,20</sup> and is expanded below.

The THz spectra for four samples of MAPbX<sub>3</sub> are shown in Figure 1c, as obtained from eqs 2 and 3. The absorbance, *A*, was small (less than 0.1 for the four perovskite samples), which can be a challenge to measure accurately in lower signal-to-noise ratio (SNR) systems. For the TF-TIR data, we plot the logarithmic reflectance, *R*<sub>log</sub> (see Methods), which was ~4 times stronger (peaking at ~0.4) and matched the spectral shape of *A*. Although the height of *A* and *R*<sub>log</sub> depends on the thickness of the film, the data presented were obtained on the same films and thus offer a direct comparison between the performance of different geometries.

For MAPbI<sub>3</sub>, a clear peak is evident at 0.96 THz in both *A* and *R*<sub>log</sub>, which can be assigned to I–Pb–I bond bending, creating distortions and twists of the inorganic octahedra,<sup>15</sup> denoted here as the “octahedral” mode. The increased absorbance/reflectance at higher frequencies is created by a second set of vibrational modes around 2 THz, attributed to the stretching of the Pb–I bond coupled to MA cations,<sup>16,21</sup> referred to as the “lurching” mode.<sup>15</sup> These vibrational modes

have been reported previously using transmission THz-TDS.<sup>16,18,21,22</sup> The observed increase in mode frequency (0.96, 0.99, 1.05, and 1.38 THz) with Br substitution is likely because of the lower average mass of the X site when Br replaces I.<sup>15</sup> However, the resonance frequency did not scale linearly with the Br content: even with the bromine concentration increasing to 1/3, the resonant frequency only had a small blue-shift and was still close to that of MAPbI<sub>3</sub>, whereas there was an abrupt change to 1.38 THz for the pure bromine MAPbBr<sub>3</sub>. This may be a result of the differing crystal system for pure MAPbBr<sub>3</sub> at room temperature, which is cubic with a space group *Pm3m*, whereas MAPbI<sub>3</sub> is tetragonal with a space group *I4/mcm*.<sup>15</sup>

To provide insights into the enhanced sensitivity in the TF-TIR geometry, consider the schematic of the experimental geometry for TF-TIR shown in Figure 1d. Here, the sample layer is a conductive thin film that is sandwiched by a rarer medium (lower refractive index, in this case, air), and a substrate that is index-matched to the prism. The sample has an optical conductance  $\sigma_{\text{sample}}$  including contributions from both free charge motion and vibrational absorption. THz light penetrates the sample to the top interface with the rarer medium, as the sample thickness is smaller than the penetration depth. The reflection coefficient (s-polarized) of this three-phase system can be written as<sup>20</sup>

$$r = \frac{n_{\text{substrate}} \cos \theta_{\text{substrate}} - n_{\text{rarer}} \cos \theta_{\text{rarer}} - Z_0 \sigma_{\text{sample}}}{n_{\text{substrate}} \cos \theta_{\text{substrate}} + n_{\text{rarer}} \cos \theta_{\text{rarer}} + Z_0 \sigma_{\text{sample}}} \quad (1)$$

where  $Z_0$  is the impedance of vacuum and  $\theta$  are the angles in the media. To compare the sensitivity of transmission, ordinary reflection (10°), and TIR geometry (37°), the THz response is given in Figure 1e,f as a function of  $\sigma_{\text{sample}}$ . The real part of  $\sigma_{\text{sample}}$  for MAPbI<sub>3</sub> peaks at 0.6 mS at the phonon resonance around 1 THz<sup>16</sup> and hence the shaded range,  $\text{Re}[\sigma_{\text{sample}}] < 2$  mS, were representative of the vibrational modes of MAPbX<sub>3</sub>. The slope marks the relative sensitivity: the ordinary reflection

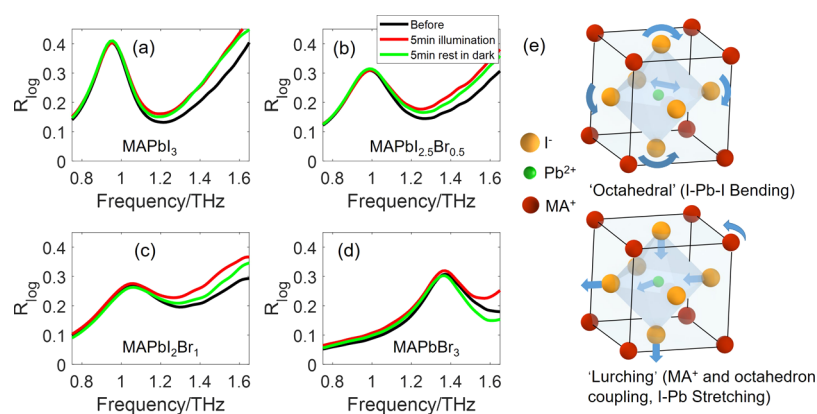


**Figure 2.** THz TF-TIR spectra before (black), after 5 min of illumination (red), and after 5 min rest in the dark (green) of CYTOP-encapsulated (a) MAPbI<sub>3</sub>, (b) MAPbI<sub>2.5</sub>Br<sub>0.5</sub>, (c) MAPbI<sub>2</sub>Br<sub>1</sub>, and (d) MAPbBr<sub>3</sub>. (e) Crystal structure of MAPbI<sub>3</sub> showing the “octahedral” and “lurching” modes.

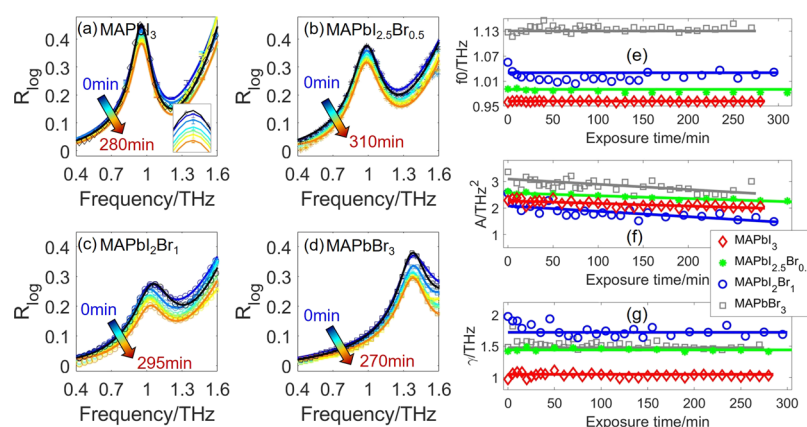


**Figure 3.** THz spectra from 0.4 to 1.6 THz of the CYTOP-encapsulated (a) MAPbI<sub>3</sub>, (b) MAPbI<sub>2.5</sub>Br<sub>0.5</sub>, (c) MAPbI<sub>2</sub>Br<sub>1</sub>, and (d) MAPbBr<sub>3</sub> samples varying with exposure times. Representative error bars are given in (a): the inset highlights the error bars around the peak. Black color indicates the spectra before the illumination. Markers are measured data and curves are fits using two Lorentzian oscillators. Fitted (e) resonant frequencies, (f) strengths, and (g) spectral widths of the “octahedral” peaks. The resonant frequencies of MAPbBr<sub>3</sub> in (e) were shifted vertically (−0.25 THz) for clarity.

geometry (10°) has the best sensitivity corresponding to the most rapid change in the measured  $R_{\log}$  with changes to  $\sigma_{\text{sample}}$ , whereas the transmission geometry has the worst sensitivity. However, the least signal is collected in the ordinary reflection spectroscopy (Figure 1f), whereas TIR yields greater amplitude, improving the SNR. The high sensitivity and SNR make THz TF-TIR geometry particularly suitable to characterize the vibrational phonon modes in perovskites during environmentally driven changes.

**Illumination Alters the “Lurching” Vibrational Modes.** The THz spectra before and after 5 min of illumination and after resting in the dark for 5 min were measured with TF-TIR for the encapsulated MAPbI<sub>3</sub>, MAPbI<sub>2.5</sub>Br<sub>0.5</sub>, MAPbI<sub>2</sub>Br<sub>1</sub>, and MAPbBr<sub>3</sub>, with the results shown in Figure 2. In all samples, short-term illumination increased the strength of the “lurching” modes, evident from the increase in  $R_{\log}$  at high frequencies, without changing the strength of the “octahedral” modes. After resting in the dark for 5 min,  $R_{\log}$  recovered partially toward its shape before light soaking, apart from the spectrum of MAPbBr<sub>3</sub>, which overshoot the original shape. Because our TF-TIR cannot measure above 1.7 THz, a CYTOP-encapsulated MAPbI<sub>2.5</sub>Br<sub>0.5</sub> sample was measured in the transmission geometry on an alternative THz-TDS system with higher bandwidth (2.5 THz), before

illumination and after 5 min of rest in the dark after the 5 min illumination. The results (Figure S1) show that the “lurching” modes at 2 THz became stronger after 5 min rest in the dark after light soaking. Supplementary PL spectra following the same illumination protocol are reported in Figure S2. However, apart from the strong phase segregation in MAPbI<sub>2</sub>Br<sub>1</sub>, PL spectra failed to reveal any effects of 5 min light-soaking on the perovskites.

We now consider possible explanations for the change in the “lurching” mode’s strength. Phase segregation<sup>11</sup> cannot be the dominant cause because it was observed for the two single halide perovskites. The combined effects of oxygen and light were ruled out by further tests on samples encapsulated in glass instead of CYTOP (because CYTOP has a perfect isolation to moisture but not to oxygen<sup>23</sup>) reported in Supporting Information Figure S3. Partial decomposition of the perovskites was excluded using XRD spectra measured before and after 5 min of light-soaking (Supporting Information Figure S4). Having ruled out these other mechanisms, we conclude that short-term illumination deforms the perovskite lattice. Illumination can rotate MA cations and reduce their binding strength to the inorganic octahedra, as evidenced by DFT calculations<sup>6</sup> and experiment.<sup>8</sup> Consequently, we presume that after illumination, the MA cations decreased its binding to the

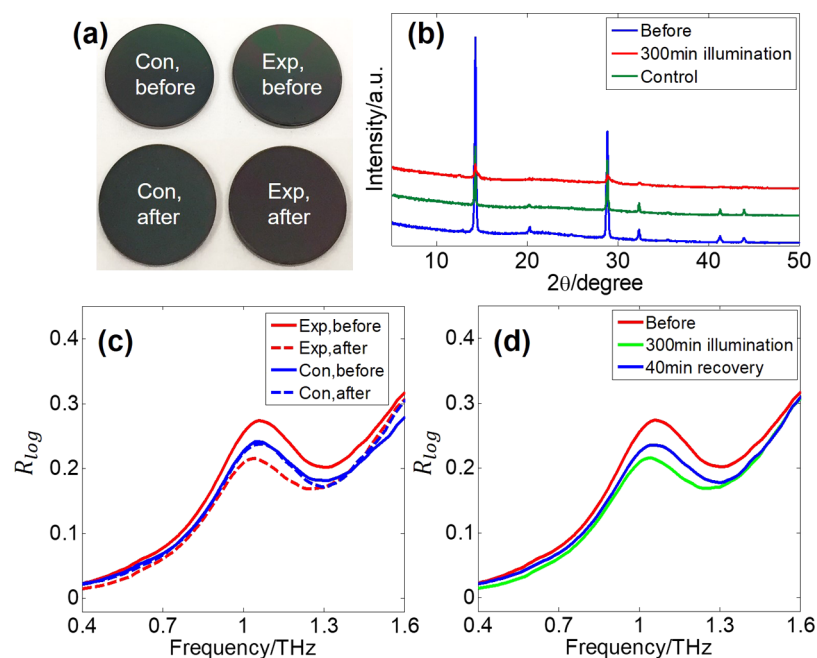


**Figure 4.** (a) Visual images, (b) XRD patterns, (c) THz TF-TIR spectra of the encapsulated  $\text{MAPbI}_2\text{Br}_1$  before, after 300 min illumination (experimental group), and after 300 min being kept in the dark (control group). The color of the sample turned brown slightly after 300 min of light soaking, which could be barely seen by the naked eye. (d) THz TF-TIR spectra of the encapsulated  $\text{MAPbI}_2\text{Br}_1$  before, after 300 min of illumination, and after recovering for 40 min in the dark.

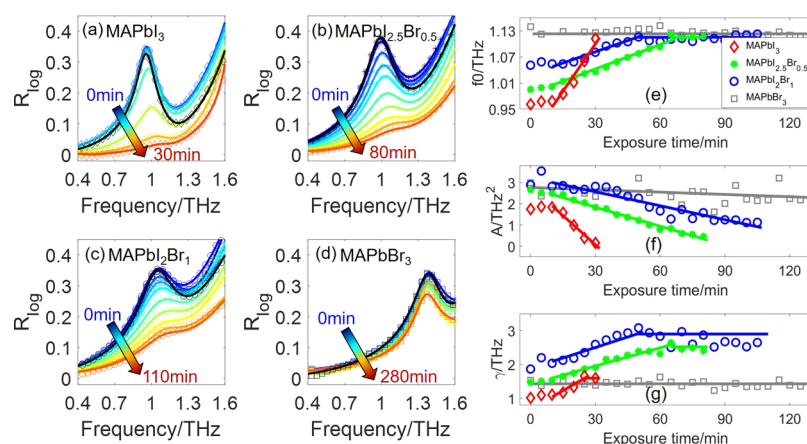


**Figure 5.** THz spectra from 0.4 to 1.6 THz of the nonencapsulated (a)  $\text{MAPbI}_3$ , (b)  $\text{MAPbI}_{2.5}\text{Br}_{0.5}$ , (c)  $\text{MAPbI}_2\text{Br}_1$ , and (d)  $\text{MAPbBr}_3$  sample varying with exposure times. Black color indicates the spectra before the illumination. Dots are measured data and curves are the two-oscillator Lorentzian fits. Fitted (e) resonant frequencies, (f) strengths, and (g) spectral widths of the “octahedral” peak over 120 min of illumination. The resonant frequencies of  $\text{MAPbBr}_3$  in (e) were shifted vertically ( $-0.25$  THz) for clarity.

octahedra, enhancing the oscillator strength of the “lurching” modes. When the light was switched off, this structural distortion recovered slowly, as the MA cations return to their original orientation and position.

**Stability of Encapsulated Films under Longer Term Illumination.** In contrast to the spectra after short-term illumination, where the “lurching” modes strengthened and the “octahedral” modes were unchanged, on longer time scales (up to 300 min) both the “octahedral” and “lurching” absorption became moderately weaker, as reported in Figure 3a–d. Representative error bars are given in Figure 3a: the light-induced spectral changes are very small even after 5 h; improving the sensitivity by TF-TIR spectroscopy made it possible to track these subtle changes in the oscillator strength. To further track these changes, the spectra were fitted by

Lorentz oscillator model (LOM, see Methods section) with two Lorentzian oscillators, and the fitted frequency  $f_0$ , amplitude  $A$ , and linewidth  $\gamma$  are shown in Figure 3e–g for the “octahedral” mode.  $\text{MAPbI}_2\text{Br}_1$  has the most significant (29%) drop in oscillator strength over 300 min compared to 12, 13, and 18% for  $\text{MAPbI}_3$ ,  $\text{MAPbI}_{2.5}\text{Br}_{0.5}$ , and  $\text{MAPbBr}_3$ , respectively. The faster degradation speed of  $\text{MAPbI}_2\text{Br}_1$  was likely caused by ion migration<sup>24</sup> in  $\text{MAPbI}_2\text{Br}_1$  because there is a more severe lattice mismatch with increasing bromine concentration.<sup>11,12,25</sup> The PL results in Figure S2 also confirmed this: the peak shift of  $\text{MAPbI}_2\text{Br}_1$  is more significant than that of  $\text{MAPbI}_{2.5}\text{Br}_{0.5}$  spectra.

To establish whether the LED illumination was the dominant cause of the long-term reduction in vibrational mode strength, a control group was stored in the dark under

the same atmospheric conditions. The visual images, XRD pattern, and THz TF-TIR spectra of a MAPbI<sub>2</sub>Br<sub>1</sub> control sample after 300 min in the dark are presented in Figure 4a–c. The control exhibited no clear difference visually or in the THz spectra. The XRD peaks lowered in intensity slightly for the control sample, indicating a reduction in crystallinity irrespective of illumination. The sample illuminated for 300 min had a more marked reduction in crystallinity and broader peaks, resulting from a reduced crystallinity of the perovskite thin film and a decreased grain size, respectively.<sup>26</sup> The reduction in strength of the THz vibrational modes is commensurate with the structural changes observed in XRD.

Furthermore, this photoinduced change was partially reversible, as evidenced in Figure 4d, for an encapsulated MAPbI<sub>2</sub>Br<sub>1</sub> sample before, after 300 min illumination, and after recovery in the dark for 40 min. This reversible effect was observed for three other compositions. The reversibility suggests that it was not the degradation into PbI<sub>2</sub> and PbBr<sub>2</sub> that caused the reduction of the peak strength.<sup>8</sup>

**Stability under Moisture, Oxygen, and Long-Term Illumination.** To explore the effects of moisture and oxygen on the vibrational modes, we conducted measurements on perovskite thin films made without encapsulation. Figure 5a–d shows the photoinduced spectral changes in the perovskites during 0–280 min of illumination with exposure to moisture, oxygen, heat, and light. In the presence of moisture, the perovskites were more sensitive to light and heat and were photomodified much quicker than the encapsulated ones.

MAPbI<sub>3</sub> presented the fastest change: after 30 min, the “octahedral” mode had totally disappeared. At this time, little of the perovskite phase remains owing to its decomposition into PbI<sub>2</sub>, MAI, CH<sub>3</sub>NH<sub>2</sub>, and I<sub>2</sub>,<sup>27,28</sup> as evidenced by visual inspection and XRD (Supporting Information Figure S5). The control samples did not degrade: in fact,  $R_{\log}$  of the control was marginally enhanced by 30 min in the dark, as explained by exposure to humid air for short time.<sup>18</sup> This portrays the highly unstable nature of MAPbI<sub>3</sub> when exposed to moisture, oxygen, and light. In contrast, for the two mixed halide perovskites, it took around 100 min before the phonon modes had vanished. After 110 min illumination, there was no clear difference visually for MAPbI<sub>2</sub>Br<sub>1</sub>, and while the XRD intensity decreased, no PbI<sub>2</sub> peak had emerged (Supporting Information Figure S5).

The spectra were fitted using the same model as above, yielding the parameters given in Figure 5e–g. During illumination, a subtle blue-shift of the lowest vibrational mode with time was observed, apart from MAPbBr<sub>3</sub>, where the oscillator strength reduced marginally. For MAPbI<sub>3</sub>, MAPbI<sub>2.5</sub>Br<sub>0.5</sub>, and MAPbI<sub>2</sub>Br<sub>1</sub>, over the 30/80/110 min of illumination, the resonant frequencies of the spectral peaks shifted from 0.96, 0.99, and 1.05 THz to around 1.11 THz (frequency shifts 0.15, 0.12, and 0.06 THz, respectively). This blue-shift with time may result from the light-induced formation of iodide vacancies, which would lower the average mass and increase the frequency of the Pb–I buckling modes. The Pb–I bond is fragile in comparison with Pb–Br:<sup>28</sup> the decomposition energy in MAPbI<sub>3</sub> is as low as 0.1 eV.<sup>29</sup> The spectral widths similarly increased with time because of the increased structural disorder.

The huge difference in deterioration rate between the encapsulated (Figure 3) and nonencapsulated (Figure 5) MAPbI<sub>3</sub> samples demonstrates that the moisture accelerates the breakdown of the structure, whereas the rate for MAPbBr<sub>3</sub>

was comparable with and without encapsulation. The better stability of the Br compound in the presence of moisture is explained by a reduced lattice constant and the transition to cubic phase, which is more stable than tetragonal phase.<sup>30</sup>

## SUMMARY

Herein, we demonstrated for the first time that THz TF-TIR spectroscopy is a sensitive method to study the vibrational modes of thin films of lead-halide perovskites. The increased sensitivity afforded by the TIR geometry allowed subtle changes in the vibrational modes associated with the inorganic octahedra and coupled Pb–X–MA modes to be explored in different environmental conditions and in-situ under illumination. From the experimental results, we deduce that there was a two-step structural change in the perovskite thin films under illumination: first, the intensity of the “lurching” modes was enhanced after 5 min of illumination; second, long-term light-soaking induced a decrease in the intensity of both “octahedral” and “lurching” phonon modes, and the “octahedral” modes had a blue shift in the presence of moisture. Our results give direct experimental evidence for the hypothesis proposed by Gottesman et al.:<sup>8</sup> inorganic octahedra realign to adapt to the rotated MA cations induced by illumination. A thorough knowledge of the vibrational modes is increasingly identified to be important because the LO phonon modes are thought to control the room-temperature charge mobility.<sup>16,31</sup> THz TF-TIR provides a novel way to study the stability of perovskites in situ and can also be used to characterize other conductive materials of interest.

## METHODS

The details of sample preparation, THz TF-TIR spectroscopy setups and measurements, and XRD and PL measurements can be found in the Supporting Information. The thickness of the perovskite samples was about 300 nm. The absorbance spectrum  $A$  of the sample is calculated from:

$$A = -2 \log_{10} \left| \frac{\text{FFT}(T_{\text{sample}}(t) \times f(t))}{\text{FFT}(T_{\text{reference}}(t) \times f(t))} \right| \quad (2)$$

where  $T_{\text{sample}}(t)$  and  $T_{\text{reference}}(t)$  are the measured THz transmission time-domain signals of the sample and the bare substrate, respectively, and  $\text{FFT}()$  denotes the Fourier transform. The filter function  $f(t)$  removed small reflections caused by the substrate and the prism interface (contact was imperfect). Similarly, we define the logarithmic reflectance  $R_{\log}$  to process the THz TF-TIR time-domain signals  $R(t)$  using

$$R_{\log} = -2 \log_{10} \left| \frac{\text{FFT}(R_{\text{sample}}(t) \times f(t))}{\text{FFT}(R_{\text{reference}}(t) \times f(t))} \right| \quad (3)$$

The measured  $A$  and  $R_{\log}$  are plotted in Figure 1 for comparison.  $R_{\log}$  is fitted by LOM to extract the oscillator strength and resonant frequency. Different from ordinary attenuated total reflection, the total reflection happens at the upper surface of the sample, and thus in TF-TIR, there is no restriction on the refractive index of the sample. The effects of the CYTOP encapsulation layer can be ignored and the detailed calculated results are given in Supporting Information Figure S6.

An LOM was used to fit the  $R_{\log}$  spectra directly, in the form shown below<sup>32</sup>

$$R_{\log} = \sum_{i=1}^N \frac{A_i}{(2\pi f_{0i})^2 - (2\pi f)^2 - j2\pi f \gamma_i} - A_{\text{off}} \quad (4)$$

where  $f_{0i}$  is the resonant frequency of the  $i$ th resonance,  $A_i$  is the strength of the  $i$ th resonance, and  $\gamma_i$  gives the information of the spectral width.  $A_{\text{off}}$  is a constant offset.  $N$  is the number of the resonances, and here we choose  $N = 2^{16,21}$  but only look at the first peak considering the spectral limitation of our TIR system. We fit the spectra in the range of 0.4–1.6 THz. Physically, in LOM fits to the permittivity of materials,  $A_i$  is positively correlated with the bound electron density of the  $i$ th resonance and  $\gamma_i$  is the phonon scattering rate.<sup>32</sup>

## ■ ASSOCIATED CONTENT

### Supporting Information

The Supporting Information is available free of charge on the ACS Publications website at DOI: 10.1021/acs.jpcc.8b05695.

THz transmission spectra before and after illumination; PL spectra before and after illumination; THz TF-TIR spectra of the glass-encapsulated perovskite before and after illumination; XRD patterns of the encapsulated MAPbI<sub>2</sub>Br<sub>1</sub> before and after illumination; THz TF-TIR spectra, visual images, and XRD patterns of the perovskites in the presence of moisture; calculated CYTOP effect on the THz spectra; sample preparation; THz TF-TIR spectroscopy setups and measurements; and XRD and PL measurements (PDF)

## ■ AUTHOR INFORMATION

### Corresponding Author

\*E-mail: e.pickwell.97@cantab.net. Phone: +44(0) 2476523981.

### ORCID

James Lloyd-Hughes: 0000-0002-9680-0138

Ni Zhao: 0000-0002-1536-8516

Emma Pickwell-MacPherson: 0000-0001-6062-5959

### Author Contributions

<sup>§</sup>Q.S. and X.L. have contributed equally to this work.

### Notes

The authors declare no competing financial interest.

## ■ ACKNOWLEDGMENTS

The authors would like to thank the research grants council of Hong Kong (project number 14201415), the Hong Kong Innovation and Technology fund (ITS/371/16), the Hong Kong PhD Fellowship award (Q.S.), and the Royal Society Wolfson Award (E.P.-M.) for the partial support of this work.

## ■ REFERENCES

- (1) Correa-Baena, J.-P.; Saliba, M.; Buonassisi, T.; Grätzel, M.; Abate, A.; Tress, W.; Hagfeldt, A. Promises and Challenges of Perovskite Solar Cells. *Science* **2017**, *358*, 739–744.
- (2) Mehmood, U.; Al-Ahmed, A.; Afzaal, M.; Al-Sulaiman, F. A.; Daud, M. Recent Progress and Remaining Challenges in Organometallic Halides Based Perovskite Solar Cells. *Renewable Sustainable Energy Rev.* **2017**, *78*, 1–14.
- (3) Kim, M.; Kim, G.-H.; Oh, K. S.; Jo, Y.; Yoon, H.; Kim, K.-H.; Lee, H.; Kim, J. Y.; Kim, D. S. High-Temperature–Short-Time Annealing Process for High-Performance Large-Area Perovskite Solar Cells. *ACS Nano* **2017**, *11*, 6057–6064.
- (4) Xiao, Z.; Kerner, R. A.; Zhao, L.; Tran, N. L.; Lee, K. M.; Koh, T.-W.; Scholes, G. D.; Rand, B. P. Efficient Perovskite Light-Emitting

Diodes Featuring Nanometre-Sized Crystallites. *Nat. Photonics* **2017**, *11*, 108.

(5) Zhu, H.; Fu, Y.; Meng, F.; Wu, X.; Gong, Z.; Ding, Q.; Gustafsson, M. V.; Trinh, M. T.; Jin, S.; Zhu, X.-Y. Lead Halide Perovskite Nanowire Lasers with Low Lasing Thresholds and High Quality Factors. *Nat. Mater.* **2015**, *14*, 636.

(6) Gottesman, R.; Haltzi, E.; Gouda, L.; Tirosh, S.; Bouhadana, Y.; Zaban, A.; Mosconi, E.; De Angelis, F. Extremely Slow Photoconductivity Response of Ch<sub>3</sub>nh<sub>3</sub>pbi<sub>3</sub> Perovskites Suggesting Structural Changes under Working Conditions. *J. Phys. Chem. Lett.* **2014**, *5*, 2662–2669.

(7) Juarez-Perez, E. J.; Sanchez, R. S.; Badia, L.; Garcia-Belmonte, G.; Kang, Y. S.; Mora-Sero, I.; Bisquert, J. Photoinduced Giant Dielectric Constant in Lead Halide Perovskite Solar Cells. *J. Phys. Chem. Lett.* **2014**, *5*, 2390–2394.

(8) Gottesman, R.; Gouda, L.; Kalanoor, B. S.; Haltzi, E.; Tirosh, S.; Rosh-Hodesh, E.; Tischler, Y.; Zaban, A.; Quarti, C.; Mosconi, E.; De Angelis, F. Photoinduced Reversible Structural Transformations in Free-Standing Ch<sub>3</sub>nh<sub>3</sub>pbi<sub>3</sub> Perovskite Films. *J. Phys. Chem. Lett.* **2015**, *6*, 2332–2338.

(9) Nie, W.; Blancon, J.-C.; Neukirch, A. J.; Appavoo, K.; Tsai, H.; Chhowalla, M.; Alam, M. A.; Sfeir, M. Y.; Katan, C.; Even, J.; et al. Light-Activated Photocurrent Degradation and Self-Healing in Perovskite Solar Cells. *Nat. Commun.* **2016**, *7*, 11574.

(10) Noh, J. H.; Im, S. H.; Heo, J. H.; Mandal, T. N.; Seok, S. I. Chemical Management for Colorful, Efficient, and Stable Inorganic–Organic Hybrid Nanostructured Solar Cells. *Nano Lett.* **2013**, *13*, 1764–1769.

(11) Hoke, E. T.; Slotcavage, D. J.; Dohner, E. R.; Bowring, A. R.; Karunadasa, H. I.; McGehee, M. D. Reversible Photo-Induced Trap Formation in Mixed-Halide Hybrid Perovskites for Photovoltaics. *Chem. Sci.* **2015**, *6*, 613–617.

(12) Slotcavage, D. J.; Karunadasa, H. I.; McGehee, M. D. Light-Induced Phase Segregation in Halide-Perovskite Absorbers. *ACS Energy Lett.* **2016**, *1*, 1199–1205.

(13) Quarti, C.; Grancini, G.; Mosconi, E.; Bruno, P.; Ball, J. M.; Lee, M. M.; Snaith, H. J.; Petrozza, A.; De Angelis, F. The Raman Spectrum of the Ch<sub>3</sub>nh<sub>3</sub>pbi<sub>3</sub> Hybrid Perovskite: Interplay of Theory and Experiment. *J. Phys. Chem. Lett.* **2014**, *5*, 279–284.

(14) Bi, D.; Yi, C.; Luo, J.; Décoppet, J.-D.; Zhang, F.; Zakeeruddin, S. M.; Li, X.; Hagfeldt, A.; Grätzel, M. Polymer-Templated Nucleation and Crystal Growth of Perovskite Films for Solar Cells with Efficiency Greater Than 21%. *Nat. Energy* **2016**, *1*, 16142.

(15) Leguy, A. M. A.; Goñi, A. R.; Frost, J. M.; Skelton, J.; Brivio, F.; Rodríguez-Martínez, X.; Weber, O. J.; Pallipurath, A.; Alonso, M. I.; Campoy-Quiles, M. Dynamic Disorder, Phonon Lifetimes, and the Assignment of Modes to the Vibrational Spectra of Methylammonium Lead Halide Perovskites. *Phys. Chem. Chem. Phys.* **2016**, *18*, 27051–27066.

(16) La-o-Vorakiat, C.; Xia, H.; Kadro, J.; Salim, T.; Zhao, D.; Ahmed, T.; Lam, Y. M.; Zhu, J.-X.; Marcus, R. A.; Michel-Beyerle, M.-E.; et al. Phonon Mode Transformation across the Orthorhombic-Tetragonal Phase Transition in a Lead Iodide Perovskite Ch<sub>3</sub>nh<sub>3</sub>pbi<sub>3</sub>: A Terahertz Time-Domain Spectroscopy Approach. *J. Phys. Chem. Lett.* **2016**, *7*, 1–6.

(17) Milot, R. L.; Eperon, G. E.; Snaith, H. J.; Johnston, M. B.; Herz, L. M. Temperature-Dependent Charge-Carrier Dynamics in Ch<sub>3</sub>nh<sub>3</sub>pbi<sub>3</sub>perovskite Thin Films. *Adv. Funct. Mater.* **2015**, *25*, 6218–6227.

(18) Park, S. J.; Kim, A. R.; Hong, J. T.; Park, J. Y.; Lee, S.; Ahn, Y. H. Crystallization Kinetics of Lead Halide Perovskite Film Monitored by In Situ Terahertz Spectroscopy. *J. Phys. Chem. Lett.* **2017**, *8*, 401–406.

(19) Liu, X.; Parrott, E. P. J.; Ung, B. S.-Y.; Pickwell-MacPherson, E. Exploiting Total Internal Reflection Geometry for Efficient Optical Modulation of Terahertz Light. *APL Photonics* **2016**, *1*, 076103.

(20) Liu, X.; Chen, Z.; Parrott, E. P. J.; Ung, B. S.-Y.; Xu, J.; Pickwell-MacPherson, E. Graphene Based Terahertz Light Modulator

in Total Internal Reflection Geometry. *Adv. Opt. Mater.* **2017**, *5*, 1600697.

(21) Wehrenfennig, C.; Liu, M.; Snaith, H. J.; Johnston, M. B.; Herz, L. M. Charge-Carrier Dynamics in Vapour-Deposited Films of the Organolead Halide Perovskite  $\text{CH}_3\text{NH}_3\text{PbI}_3$ -Xclx. *Energy Environ. Sci.* **2014**, *7*, 2269–2275.

(22) Zhao, D.; Skelton, J. M.; Hu, H.; La-o-vorakiat, C.; Zhu, J.-X.; Marcus, R. A.; Michel-Beyerle, M.-E.; Lam, Y. M.; Walsh, A.; Chia, E. E. M. Low-Frequency Optical Phonon Modes and Carrier Mobility in the Halide Perovskite  $\text{CH}_3\text{NH}_3\text{PbBr}_3$  Using Terahertz Time-Domain Spectroscopy. *Appl. Phys. Lett.* **2017**, *111*, 201903.

(23) Harwell, J. R.; Whitworth, G. L.; Turnbull, G. A.; Samuel, I. D. W. Green Perovskite Distributed Feedback Lasers. *Sci. Rep.* **2017**, *7*, 11727.

(24) Nandal, V.; Nair, P. R. Predictive Modeling of Ion Migration Induced Degradation in Perovskite Solar Cells. *ACS Nano* **2017**, *11*, 11505–11512.

(25) Yuan, Y.; Huang, J. Ion Migration in Organometal Trihalide Perovskite and Its Impact on Photovoltaic Efficiency and Stability. *Acc. Chem. Res.* **2016**, *49*, 286–293.

(26) Li, Z. Y.; Lam, W. M.; Yang, C.; Xu, B.; Ni, G. X.; Abbah, S. A.; Cheung, K. M. C.; Luk, K. D. K.; Lu, W. W. Chemical Composition, Crystal Size and Lattice Structural Changes after Incorporation of Strontium into Biomimetic Apatite. *Biomaterials* **2007**, *28*, 1452–1460.

(27) Niu, G.; Guo, X.; Wang, L. Review of Recent Progress in Chemical Stability of Perovskite Solar Cells. *J. Mater. Chem. A* **2015**, *3*, 8970–8980.

(28) Misra, R. K.; Aharon, S.; Li, B.; Mogilyansky, D.; Visoly-Fisher, I.; Etgar, L.; Katz, E. A. Temperature- and Component-Dependent Degradation of Perovskite Photovoltaic Materials under Concentrated Sunlight. *J. Phys. Chem. Lett.* **2015**, *6*, 326–330.

(29) Buin, A.; Pietsch, P.; Xu, J.; Voznyy, O.; Ip, A. H.; Comin, R.; Sargent, E. H. Materials Processing Routes to Trap-Free Halide Perovskites. *Nano Lett.* **2014**, *14*, 6281–6286.

(30) Noh, J. H.; Im, S. H.; Heo, J. H.; Mandal, T. N.; Seok, S. I. Chemical Management for Colorful, Efficient, and Stable Inorganic-Organic Hybrid Nanostructured Solar Cells. *Nano Lett.* **2013**, *13*, 1764–1769.

(31) Herz, L. M. Charge-Carrier Mobilities in Metal Halide Perovskites: Fundamental Mechanisms and Limits. *ACS Energy Lett.* **2017**, *2*, 1539–1548.

(32) Parrott, E. P. J.; Zeitler, J. A.; McGregor, J.; Oei, S.-P.; Unalan, H. E.; Tan, S.-C.; Milne, W. I.; Tessonier, J.-P.; Schlögl, R.; Gladden, L. F. Understanding the Dielectric Properties of Heat-Treated Carbon Nanofibers at Terahertz Frequencies: A New Perspective on the Catalytic Activity of Structured Carbonaceous Materials. *J. Phys. Chem. C* **2009**, *113*, 10554–10559.